RESEARCH ARTICLE MANUSCRIPT

Transport Phenomena and Fluid Mechanics

Simulation of the liquid flow distribution in laboratory-scale additively manufactured packings

Nadin Sarajlic[1] | Johannes Neukäufer[2] | Mohamed Adel Ashour[2] | Thomas Grützner[2] | Sebastian Meinicke[3] | Carsten Knösche[3] | Jürgen Paschold[3] | Harald Klein[1] | Sebastian Rehfeldt[1]

[1]Technical University of Munich, TUM School of Engineering and Design, Department of Energy and Process Engineering, Institute of Plant and Process Technology, 85748 Garching, Germany

[2]Ulm University, Institute of Chemical Engineering, Laboratory of Thermal Process Engineering, 89081 Ulm, Germany

[3]BASF SE, 67056 Ludwigshafen am Rhein, Germany

Correspondence
Nadin Sarajlic, Technical University of Munich, TUM School of Engineering and Design, Institute of Plant and Process Technology, 85748 Garching, Germany
Email: nadin.sarajlic@tum.de

This paper demonstrates that a newly designed packing structure can be additively manufactured, and that a more uniform liquid distribution is achieved with it. Preliminary computational fluid dynamics simulations eliminate the necessity to manufacture every developed geometry when optimizing packing structures. This work simulates the liquid flow inside two packing structures with an enclosing wall at laboratory scale. The periodic setup permits simulations of the liquid distribution in a large part of the column even for complex packing structures. A novel method for the systematic evaluation of the liquid distribution is applied to the simulation results and subsequently validated with experimental data. The results are used to improve the liquid distribution inside laboratory-scale packing structures.

KEYWORDS
additive manufacturing, CFD simulation, liquid distribution, scale-up, structured packings

Abbreviations: AM, additive manufacturing; BC, boundary condition; CFD, computational fluid dynamics; RP9M, Rombopak 9M; RP9M-3D, 3D printable Rombopak 9M; VOF, volume of fluid.

1 | INTRODUCTION

Distillation is one of the most important thermal separation processes. It is realized using tray or packed columns. As packed columns have a higher capacity and lower pressure drop than tray columns, they are used increasingly in the chemical industry. [1]

Packed columns can be implemented with structured or random packings, where the former, by definition, possess a more homogeneous form than the latter. At the industrial scale, these packings can attain diameters of several meters, resulting in high capital and operating costs. Although the software for process simulation is ever-improving, experimental data on separation performance is still indispensable. Therefore, the design of distillation columns for a new separation task yet involves laboratory-scale tests. The diameter of these columns usually ranges from 30 to 80 mm. Separation performance data acquired with these columns is used for scale-up to industrial-scale columns [2].

For the scale-up process, detailed knowledge of packing performance under various conditions is needed. Packings with high and constant separation efficiency over broad operating ranges are particularly advantageous [1]. A small diameter of down to 20 mm is especially beneficial because the smaller size reduces the manufacturing and operating costs of test rigs by, e.g., decreasing the amount of substance needed for experiments [3]. However, smaller diameter columns result in a disproportionate increase in wall effects such as heat loss and the tendency of the liquid to flow towards the column wall [4]. This maldistribution effect can lower the separation efficiency of packing structures significantly which severely limits the transferability of the results and therefore increases the difficulty of the scale-up process [5].

By contrast, a uniform distribution of the liquid inside the column leads to higher separation efficiencies and is thus the objective when designing new packing geometries [6]. However, for the small-diameter packings used at laboratory scale, conventional manufacturing methods reach their design limits if scalability of the packings is to be maintained. Moreover, the production of these laboratory packings involves manual work which in turn results in high production costs.

Additive manufacturing (AM) offers a solution to these problems because it considerably enhances both the freedom of design and the production speed of packing geometries [7]. In chemical engineering, AM has, amongst

other things, been used for reaction chemistry [8], rotating packed beds [9] and absorption [10]. In addition, 3D-printed structured packings and distillation columns have recently been investigated [3, 11, 12]. As AM can be used to generate highly homogeneous geometries [13], it represents a new tool for designing innovative structured packings for distillation columns ensuring uniform liquid distribution, decreased wall flows and higher separation efficiencies even at a laboratory scale.

Since AM opens up a wide range of packing design possibilities, preceding simulations of the liquid distribution inside the structures become essential. Computational fluid dynamics (CFD) simulations can be utilized to estimate the pressure drop, mass transfer and liquid distribution. Holdup and effective area can be calculated to enhance the dimensioning of columns. CFD simulations can also be used to improve complex apparatuses like dividing wall columns [14]. Several papers relating to CFD simulations inside structured packings exist. Said et al. [15] and Lautenschleger et al. [16] investigate the gas-phase flow inside structured packings. The latter describe a method to determine the dry pressure drop and estimate the mass transfer inside a packing.

Bertling et al. [17] use the volume of fluid (VOF) method introduced by Hirt and Nichols [18] to simulate the liquid flow over micro-structured surfaces. Haroun et al. [19] and Olenberg and Kenig [20] use CFD simulations of the liquid flow to determine the effective area and liquid holdup inside a section of structured packings. Ataki and Bart [21] investigate the liquid flow over a similar packing structure as is done in this contribution, however, they only simulate a single packing element.

With the Generalised Continuous Species Transfer model, Hill et al. [22] introduce a method to couple the two-phase flow inside a packing with a simulation of the species transfer. This enables the determination of the *HETP* value inside a packing. Macfarlan et al. [23] investigate the mass transfer of structured packings in the gas phase and validate the results using an SO_2 scrubbing process with a conventional packing. Furthermore, the group recently published a paper which investigates the influence of the structured packing geometry on the liquid phase performance. They emphasize the importance of the channel inclination angle regarding the mass transfer [24].

While Olenberg and Kenig [20], Hill et al. [22] and Macfarlan et al. [23, 24] use cyclic boundary conditions (BC) to decrease restrictions due to computing resources while still representing a large part of the packing, neither of the simulation frameworks includes the column wall. As stated above, inside laboratory-scale columns, the effects of the

column wall increase disproportionally with decreasing diameter. Reitze et al. [25] recently investigated the radial liquid distribution inside additively manufactured laboratory-scale packings and concluded that the structures should be optimized to redirect the liquid flow into the packing structure. Therefore, a method capturing these effects while allowing for the simulation of a large part of the packing using a periodic setup is important.

A setup for simulating the liquid flow inside a packing at laboratory scale with a packing diameter of $D = 20\,\mathrm{mm}$ using cyclic boundary conditions is presented in this paper. The objective of the presented method is the simulation of a packing segment inside a long column without allowing for the influence of the effects of flow development. An efficient data processing method is developed for the analysis of the liquid distribution. The simulation results are compared to experimental data.

2 | SIMULATION METHOD

2.1 | Fluid dynamics

The applied simulation method is based on the transient, isothermal two-phase flow solver `interFoam` (OpenFOAM, v1906 [26]). The fluid flow is described by solving the Navier-Stokes equations (1) and (2) [27]. For an incompressible fluid as assumed in this work, mass conservation is represented by the following equation:

$$\nabla \cdot \mathbf{u} = 0\,. \tag{1}$$

Momentum conservation is described by the following equation:

$$\rho \cdot \frac{\partial \mathbf{u}}{\partial t} + \rho \cdot \nabla \cdot (\mathbf{u} \cdot \mathbf{u}) = -\nabla \cdot p + \nabla \cdot \tau + \rho \cdot \mathbf{g}\,. \tag{2}$$

This paper deals with an application that is primarily characterized by film flow with a predominantly continuous gas-liquid interface. The dispersion of one phase into the other is assumed not to be relevant. Therefore, volume of fluid (VOF) is the method of choice. Using the VOF method introduced by Hirt and Nichols [18], a single set of equations is solved for both phases. The computation of the gas-liquid interface is part of the solution. However, in the VOF method, the exact location of the interface is unknown. It is not defined as a boundary, rather taken into account by

determining the fraction of each phase inside the considered cells (*interface-capturing method*). A liquid-filled cell has a liquid fraction value of $\alpha = 1$, whereas a gas-filled cell has $\alpha = 0$. Cells with values of $0 < \alpha < 1$ mark the gas-liquid interface. Compared to other free surface treatment methods, e.g., the *Marker-and-Cell* method, VOF is an efficient approach for simulating flows containing two immiscible fluids and treating complex interface shapes. Haroun et al. [19] show that the liquid flow over structured packings is well predicted using the VOF method. However, as the interface is not sharply defined but spread over several cells, cell refinement in areas with liquid fractions $0 < \alpha < 1$ is crucial to achieve accurate simulation results [27].

In addition to the mass and momentum conservation Equations (1) and (2), a transport equation [28, 29] is solved:

$$\frac{\partial \alpha}{\partial t} + \boldsymbol{\nabla} \cdot (\mathbf{u} \cdot \alpha) = 0\,. \tag{3}$$

As the gas-liquid interface is not treated as a boundary, fluid properties are calculated assuming a single fluid with changing characteristics at the interface:

$$\rho = \rho_l \cdot \alpha + \rho_g \cdot (1 - \alpha) \tag{4}$$

$$\mu = \mu_l \cdot \alpha + \mu_g \cdot (1 - \alpha), \tag{5}$$

where the index g denotes the gas-phase and l the liquid-phase. Mass transfer between the gas and liquid phase is assumed to be zero.

To reduce problems that arise due to the convection of the step-function induced by the use of the liquid fraction, the interface is compressed by the following equation:

$$\frac{\partial \alpha}{\partial t} + \nabla \cdot (\mathbf{u} \cdot \alpha) + \nabla \cdot \left[\mathbf{u}_r \cdot \alpha \cdot (1 - \alpha)\right] = 0\,. \tag{6}$$

The term $\alpha \cdot (1 - \alpha)$ ensures that the compression is only active within the numerical representation of the interface, i.e., at α values between 0 and 1, while $\mathbf{u}_r$ is chosen as a velocity field that is suitable for the compression [30].

Occurring effects like the surface tension are considered by adding a body force $\mathbf{f}$ to the momentum conservation equation:

$$\rho \cdot \frac{\partial \mathbf{u}}{\partial t} + \rho \cdot \nabla \cdot (\mathbf{u} \cdot \mathbf{u}) = -\nabla \cdot p + \nabla \cdot \tau + \rho \cdot \mathbf{g} + \mathbf{f}\,. \tag{7}$$

Using the *continuum surface force* approach introduced by Brackbill et al. [31], the body force $\mathbf{f}_\sigma$ representing the surface tension can be expressed as:

$$\mathbf{f}_\sigma = \sigma \cdot \kappa \cdot \nabla\alpha \tag{8}$$

with κ being the curvature of the interface [27, 29]:

$$\kappa = -\nabla \cdot \left(\frac{\nabla\alpha}{|\nabla\alpha|} \right). \tag{9}$$

As the gradient of the liquid fraction α equals zero inside the liquid and gas bulk, the body force $\mathbf{f}_\sigma$ in Eq. (8) solely applies at the interface.

The two-phase flow is modeled with a stagnant gas phase and a liquid phase that is accelerated downwards by gravity. Unless operating conditions are near the loading point, liquid holdup can be assumed to be independent of gas velocity, yielding a simulation that does not incorporate gas counter-current-flow [6]. Furthermore, the liquid flow is assumed to be laminar in accordance with Ataki and Bart [21].

The liquid flow inside the packing structures is simulated with cyclic boundary conditions, as mentioned above. Therefore, it is not possible to apply velocity inlet and pressure outlet BCs as done by Ataki and Bart [21]. This is solved by adding another body force to Equation (7):

$$\mathbf{f}_G = \rho_g \cdot \mathbf{g}. \tag{10}$$

Thus, the hydrostatic pressure gradient is no longer simulated. However, this modification is necessary to enable copying of the pressure of the lower domain end to the upper end [32]. As it is not possible to specify an inlet velocity, the liquid inside the structure is initialized in a stagnant state and is then accelerated by gravity until a balance between friction and gravitational forces is reached. This results in a liquid distribution inside the packing, with an average velocity, that strives for a (quasi-) steady state.

The interaction between the liquid and the solid surface has a major influence on the liquid flow over the structure and its wetting. The contact angle, which is the angle that forms at the contact point of liquid, gas and solid, is dynamically calculated [33]. A static contact angle (Θ_0) for stagnant fluid as well as an advancing (Θ_A) and a receding (Θ_R) contact angle (see Fig. 1) for liquid in motion have to be defined. The contact angle Θ is then calculated according to:

$$\Theta = \Theta_0 + (\Theta_A - \Theta_R) \cdot \tanh\left(\frac{u_S}{u_\Theta}\right), \tag{11}$$

with a defined velocity scaling u_Θ and the velocity u_S at the solid surface, which is part of the solution [34].

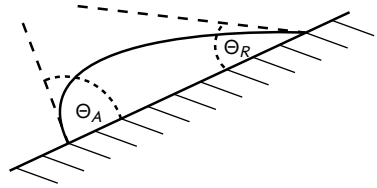

FIGURE 1 Advancing (Θ_A) and receding (Θ_R) contact angle in a moving droplet.

2.2 | General case setup

The simulation domain is subdivided into cells, the mesh. A hexahedral background mesh defines the extent of the domain which has a diameter of $D = 20\,\text{mm}$. The OpenFOAM utility `snappyHexMesh` refines the mesh around the packing geometry that is defined by a file in stereolithography (STL) format and removes cells that are entirely enclosed by the geometry. Parameters defining, amongst other things, the refinement steps, are specified in a dictionary file. These are, e.g., the surface refinement level, which specifies how often a cell is split during the refinement phase, and the number of cell layers between a refined and an unrefined cell. This approach generates a mesh that is coarse in the fluid bulk phase while finer cells are located close to the packing surface, where the gas-liquid interface is generally found (see Fig. 2). The mesh represents the fluid (colored with liquid fraction α) that is enclosed by packing geometry and column wall (gray). Especially narrow gaps between solid surfaces as shown on the right side of Fig. 2 need to be carefully refined. There, liquid tends to accumulate and form a curved interface.

The first order, bounded implicit `Euler` scheme is chosen for the discretization of the time derivative [26]. The time step size is variably set by the solver and is constrained by the Courant number

$$\text{Co} = \frac{\Delta t}{\frac{\Delta \mathbf{x}}{\mathbf{u}}}. \tag{12}$$

It describes the simulated time step Δt relative to the time $\Delta\mathbf{x}/\mathbf{u}$ that a disturbance takes to cross the distance $\Delta\mathbf{x}$, which is determined by the grid size of the domain [27]. For the conducted simulations, $\text{Co} \leq 1$ is specified. To avoid

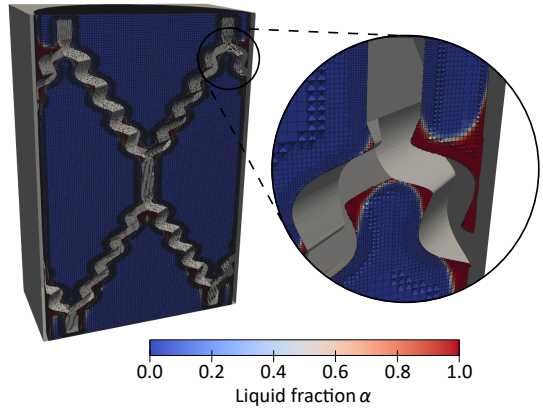

FIGURE 2 Meshed fluid (colored with liquid fraction α) and packing geometry (gray) with smaller cells near the solid surfaces.

an unphysical solution, Ferziger et al. [27] state that Co $<$ 1 needs to be satisfied for simulations where diffusion is negligible. Simulations at a lower Courant number (Co $\leq$ 0.3 is used by way of example) result in small deviations, while the simulation time is approximately tripled, meaning that there is a trade-off between accuracy and simulation speed.

The previously mentioned BCs for pressure and velocity at the upper and lower end of the simulation domain are implemented in a cyclic manner. For this purpose, the BC `cyclicAMI` that is available in OpenFOAM is used. It is also applied to the liquid fraction α. The contact angles at the wall are defined using the `dynamicAlphaContactAngle` BC. For pressure and velocity at the wall, a `fixedFluxPressure` BC with a gradient of 0 and a `fixedValue` BC with a value of 0 are defined, respectively.

Inside the fluid, pressure and velocity are initialized with values of $p = 1 \times 10^5$ Pa and $u = 0\,\mathrm{m\,s^{-1}}$. Due to the cyclic boundary conditions, a certain liquid volume flow $\dot{V}_l$ or, preferably, liquid load

$$L_{\mathrm{overall}} = \frac{\dot{V}_l}{A_{0,\mathrm{overall}}} \tag{13}$$

referring to the empty column cross section $A_{0,\mathrm{overall}}$ cannot be specified. However, it is possible to set a certain liquid holdup which yields a mean liquid velocity and therefore a liquid load L_{overall} that is part of the solution and varies with the simulated geometry. The simulations are performed with varying initial holdups until the desired liquid load L_{overall} is reached. This iterative approach is necessary to approximate the desired liquid load L_{overall}. As a simplification, the liquid inside the domain is initialized in the form of a disc with a diameter matching the simulation domain to ensure a

uniform initial liquid distribution over the cross section. The simulation is executed, until the effect of the initial liquid distribution vanishes.

2.3 | Simulation data processing

Using an OpenFOAM `functionObject`, the liquid flux through the outlet is continuously logged and used to calculate the liquid load. As previously described, the average velocity of the liquid flow strives for a steady state which cannot be calculated in advance. The duration until a quasi-steady state is reached, depends, amongst other things, on the geometry. When a quasi-steady state is reached, the simulation is terminated.

As stated above, a uniform liquid distribution over the cross section of the packing is crucial in achieving high separation efficiencies. For a systematic evaluation of the liquid distribution inside the packing, the liquid load at the bottom of the domain is determined. Top and bottom of the domain are divided into four rings that are, except for the inner circle, subdivided into four segments (see Fig. 3). Each of the thirteen resulting bottom segments is connected to its corresponding segment at the top with a cyclic BC. The number and size of the segments can be freely selected, thus allowing for an arbitrary subdivision of the outlet. The chosen segmentation matches the experimental setup that is described in Section 3.3.

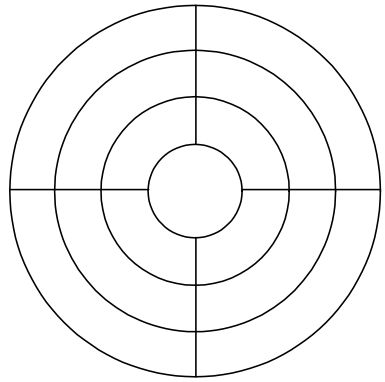

FIGURE 3 Segmented bottom of the simulation domain.

A MATLAB script is used to read and process the logged data [35]. As the liquid flux through the outlet is tracked at

every time step, average values over user-specified time intervals are calculated to minimize the impact of fluctuations. To determine the local liquid load L_i for each individual segment, the average liquid flux is divided by the corresponding empty segment area $A_{0,i}$.

Alternatively, this approach can be applied to volume segments of the same cross section and domain height. During runtime, a `functionObject` is utilized to sample the liquid fraction α in each cell of the considered volume segment and to calculate the volume average over the segment which equals its liquid holdup h_i. Furthermore, the velocity field $\mathbf{u}_i$ of each segment is extracted and a volume average of the axial velocity component that is weighted with the liquid fraction α_i is determined. With MATLAB, the product of the holdup h_i and the average velocity $u_{\text{avg},i}$ is calculated resulting in a volume averaged liquid load over each volume segment.

The division of the domain into segments allows for a simple evaluation of the liquid distribution over the outlet. However, the small packing diameter of 20 mm inevitably leads to maldistribution of the solid parts of the packing, here referred to as packing crosspieces, and hollow spaces over the segments. Furthermore, the influence of the column wall cannot be omitted. In large-scale columns, the evaluated segments would be significantly larger resulting in a more uniform distribution of the geometry over the segments in average. As a consequence, at small scale, local liquid loads cannot be utilized on their own to evaluate whether liquid is unevenly distributed due to disadvantageous wetting or due to inhomogeneous geometry distribution.

Therefore, the optimal local liquid load $L_{\text{opt},i}$ for each segment i considering the share of contained packing crosspieces is determined:

$$L_{\text{opt},i} = L_{\text{overall}} \cdot \frac{C_{\text{CP},i}}{C_{\text{CP,overall}}} \cdot \frac{A_{0,\text{overall}}}{A_{0,i}} \,. \tag{14}$$

The more packing crosspiece or wall (index CP) circumference a segment contains, the higher the optimal local liquid load $L_{\text{opt},i}$ is. Therefore, the liquid load L_{overall} over the whole outlet at quasi-steady state is multiplied with the relative packing crosspiece or wall circumference $C_{\text{CP},i}/C_{\text{CP,overall}}$. It is divided by the relative segment area $A_{0,i}/A_{0,\text{overall}}$ (referring to column cross section) to correct the varying segment areas. Since the wall contains a large proportion of the mass transfer area when the diameter is small, it must be included in the calculation. Figure 4 shows a typical plot used in evaluating the transient local liquid load L_i over segment i (solid line) and the corresponding optimal local liquid

load $L_{\text{opt},i}$ (dashed line) in a quasi-steady state. This can be used to compare the actual liquid load in a segment with the liquid load that would result if the packing crosspieces and the column wall were evenly wetted assuming uniform film thickness and liquid velocity.

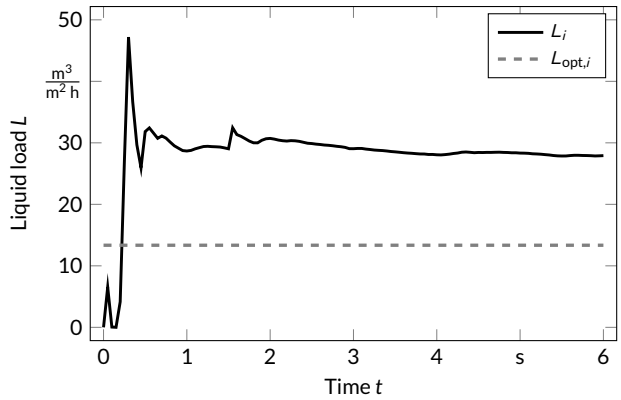

FIGURE 4 Local liquid load L_i over time (solid line) and optimal local liquid load $L_{\text{opt},i}$ (dashed line) in a quasi-steady state over a segment i.

3 | RESULTS AND DISCUSSION

3.1 | Application of the simulation approach

The simulation technique described in the previous section is applied to the two additively manufactured packing geometries shown in Figure 5. The left side of Figure 5 shows a 3D printable version of the Rombopak 9M (RP9M) from Kühni/Sulzer [36]. The RP9M is a conventionally manufactured structured packing with advantageous scale-up properties that is used in laboratory-scale distillation columns. It has been parameterized to allow easy modification of the geometry and has been printed with thicker packing crosspieces to enable the additive manufacturing of the structure, resulting in the RP9M-3D [3]. The right side of Figure 5 depicts the new packing structure XW-Pak which adopts elements of the RP9M-3D while having a generally less anisotropic structure.

The geometric features of the investigated packings are summarized in Table 1. Both structures have a diameter D of 20 mm, comparable specific geometric surface areas $a_{\text{geo, P}}$ (excluding the wall), and similar void fractions ε. This

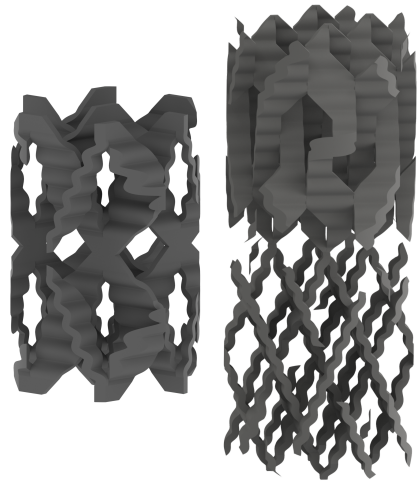

FIGURE 5 Simulated packing geometries: 3D printable Rombopak 9M (RP9M-3D, left) and XW-Pak (right).

enables the comparison of the separation efficiencies of the structured packings. A single layer of RP9M-3D is 30.8 mm high, while one layer of the XW-Pak has a height H of 50.8 mm. Neukäufer et al. [3] present detailed features of the RP9M-3D.

TABLE 1 Packing dimensions of RP9M-3D and the XW-Pak

Parameter	RP9M-3D	XW-Pak
Height H in mm	30.8	50.8
Diameter D in mm	20	20
Spec. geom. surface area $a_{geo,P}$ in $m^2\ m^{-3}$	355	351
Void fraction ε in %	88.2	88.7

In the simulations, fluid properties of *n*-heptane are applied for the liquid phase, while air is assumed to be the gas phase (see Tab. 2). Measurements made in a simplified experimental setup similar to that of Macdougall and Ockrent [37] using isohexane (which has similar fluid properties to *n*-heptane) were used as an approximation for the contact angles of *n*-heptane (see Tab. 2). As organic solvents tend to strongly wet solid surfaces, a precise measurement of the contact angles of *n*-heptane is problematic [38]. Therefore, the measured value of the static contact angle Θ_0 is applied, while the measurements of the advancing and receding contact angles as well as the velocity scaling were approximated

TABLE 2 Fluid properties of the simulated system air/*n*-heptane [39, 40]

Parameter	Air	*n*-Heptane
Kin. viscosity ν in $m^2\,s^{-1}$	1.48E-05	6.10E-07
Density ρ in $kg\,m^{-3}$	1.00	683.75
Surface tension σ in $kg\,s^{-2}$	0.02053	
Stat. contact angle Θ_0 in °	10.0	
Adv. contact angle Θ_A in °	11.8	
Rec. contact angle Θ_R in °	1.0	
Velocity scaling u_Θ in $m\,s^{-1}$	0.1	

as auxiliary values to ensure a stable simulation. While the assumed values may slightly differ from exact values, they can still be used to compare simulation data for different packing geometries as the transferability of the results is maintained.

The simulations are initialized with a defined stagnant liquid holdup. The liquid flow through the packings is simulated until a quasi-steady state of the liquid flow through the domain boundaries is reached. The quasi-steady state is reached when the variation of the mean overall liquid load during a time period of 0.1 s drops beneath 5 %. For both geometries, this is achieved after approximately 5 s of simulation time. The simulation results are evaluated after another second using the data processing tools described in Section 2.3. The additional second is required for a mesh independence study.

The selection of a suitable mesh is a compromise between the high accuracy of a fine numerical grid and the short simulation time of a coarse numerical grid. Therefore, the simulations of the RP9M-3D were performed with four meshes having different levels of refinement to investigate the mesh sensitivity of the results. The meshes differ in the level of surface refinement and the number of cells used for the transition between two differently sized cell layers. Table 3 summarizes the numbers of cells of the four investigated meshes as well as the input parameters for the `snappyHexMeshDict` in OpenFOAM. The background mesh has a cell length of 0.2 mm in all three dimensions.

A base simulation using Mesh 1 was run until a quasi-steady state was reached after $t = 5$ s. The solution of the pressure, velocity and liquid fraction field was mapped onto the finer meshes 2 – 4 using the OpenFOAM utility `mapFields`. All four cases were then simulated for a further second, yielding new quasi-steady states with the finer

TABLE 3 Number of cells, surface refinement levels and number of cells between layers for the four utilized meshes

Mesh	Cells	Surf. ref. level	Cells b. layers
1	2.11E+06	(1 1)	2
2	6.78E+06	(2 2)	2
3	1.17E+07	(2 2)	4
4	2.58E+07	(3 3)	2

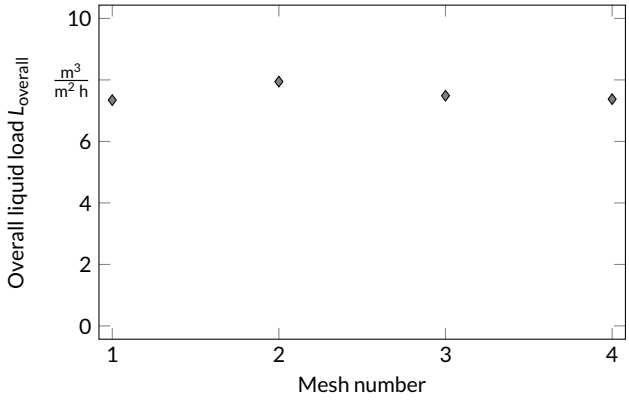

FIGURE 6 Overall liquid load $L_{overall}$ in quasi-steady state for the different meshes.

meshes.

Figure 6 shows the overall liquid load $L_{overall}$ in the quasi-steady state in relation to the operating range of the laboratory column of Neukäufer et al. [3]. The global liquid load varies only slightly for the different meshes with a maximum relative deviation of less than 8 % from the finest mesh.

The local liquid loads L_i over the 13 segments resulting from the four meshes are depicted in the upper part of Figure 7. The lower part of Figure 7 shows the liquid fraction α over the bottom end of the domain for each mesh as well an enlarged view of the liquid fraction at the wall for Mesh 1 and Mesh 3. The liquid fraction distribution itself does not change significantly. However, the film in, e.g., the upper left outer ring quarter segment (indicated by the red arrow) decreases from Mesh 1 to Mesh 3. This leads to a lower local liquid load L_i in this segment. On the other hand, the film in the upper right quarter segment of the outer ring (indicated by the yellow arrow) is thicker for Mesh 3 than for Mesh 1 resulting in a higher local liquid load L_i. The described effect is strongest when refining Mesh 1. The local liquid loads L_i of Mesh 1 deviate significantly from the other three meshes, while the results for Mesh 2–4 are a better

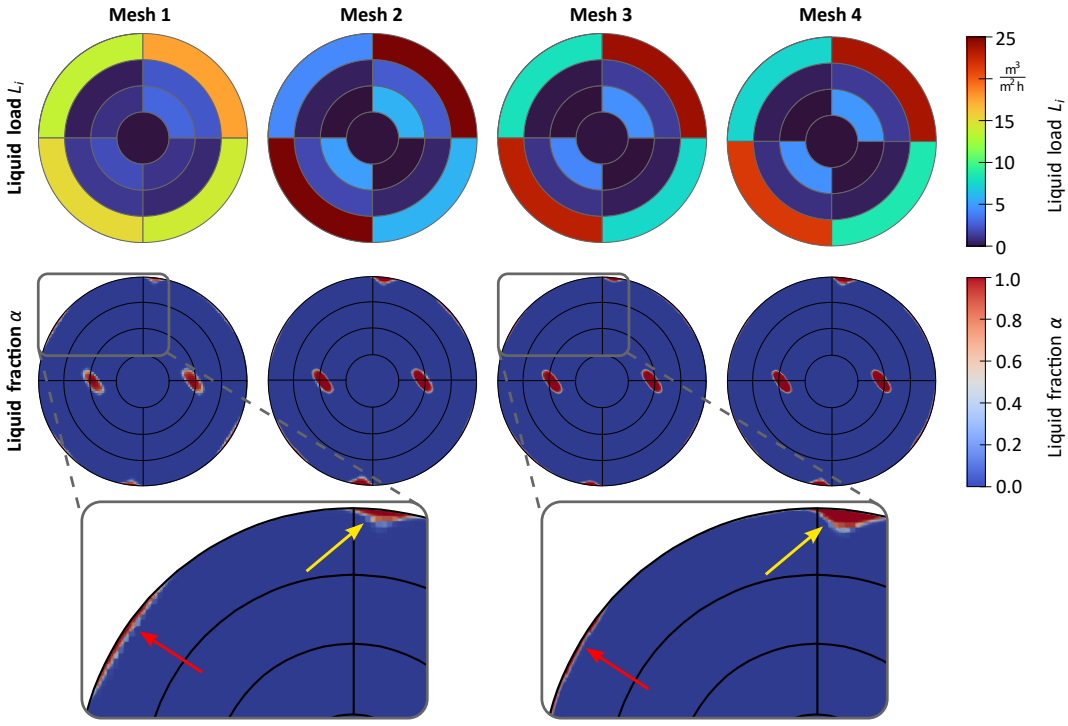

FIGURE 7 Liquid load L_i over the segments (top) and liquid fraction α (bottom) for each mesh.

match. While the deviations between Meshes 2 and 3 remain pronounced, the differences between Meshes 3 and 4 are only slight. This is also supported by a more detailed analysis of the relative deviations. Using the same number of cores, the calculations require approximately ten times more computing time using Mesh 2 than when using Mesh 1. The time needed doubles when using Mesh 3 instead of Mesh 2. For a first screening of liquid load distributions in different packing structures, the results of Mesh 2 would be sufficient. However, Mesh 3 is used for further evaluations to yield more accurate results with a tolerable computing time of approximately 20 days using 112 cores (core nominal frequency: 2.6 GHz). The `mapFields`-utility proves to be a valuable tool in reducing computational time even further by utilizing a converged simulation with a coarser mesh as a starting point.

3.2 | Simulation results

Figure 8 by way of example depicts the packing structure RP9M-3D (gray) and the resulting liquid distribution colored by the magnitude of the liquid velocity $|u_{\text{liq}}|$. The overall liquid load amounts to $L_{\text{overall}} \approx 7.5\,\text{m}^3\,\text{m}^{-2}\,\text{h}^{-1}$ for RP9M-3D and in $L_{\text{overall}} \approx 6.8\,\text{m}^3\,\text{m}^{-2}\,\text{h}^{-1}$ for the XW-Pak. These liquid loads lie within a suitable operating range for laboratory-scale columns and match the setup of Neukäufer et al. [3]. This range is adequate to allow conclusions to be drawn from the simulation results for subsequent application to experiments.

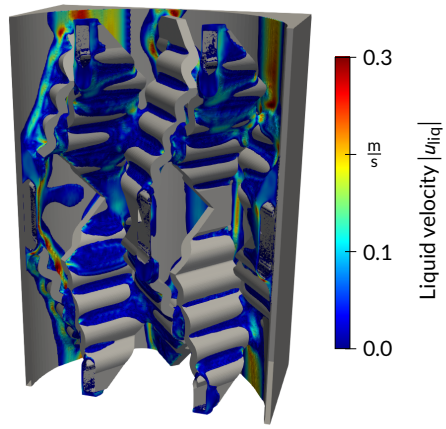

FIGURE 8 Liquid distribution inside the packing structure RP9M-3D (gray) colored by the magnitude of the liquid velocity $|u_{\text{liq}}|$.

Figure 9 shows the local liquid load L_i over the thirteen segments for the RP9M-3D (top) and the XW-Pak (bottom) on the left. The optimal local liquid load $L_{\text{opt},i}$ over each segment according to Eq. (14) is depicted in the center. The deviation $\Delta L_{\text{opt},i}$ of the liquid load L_i from the optimal liquid load $L_{\text{opt},i}$ is shown on the right.

Both packings tend to direct the liquid towards the wall, which is a general problem of small-scale packings due to the high wall-to-core ratio [41]. Furthermore, the liquid is shown to favor two quarter segments of the cross section in both cases; this results from the asymmetric design of the geometries (see Fig. 5). The optimal liquid load $L_{\text{opt},i}$ in the outer ring of both packings is higher than in the inner rings because the circumference of the wall is also considered in the calculations and takes up a large part of the structure surface area. The XW-Pak has more segments with a deviation $\Delta L_{\text{opt},i}$ of almost zero and, therefore, matches its optimal liquid load distribution with respect to the packing

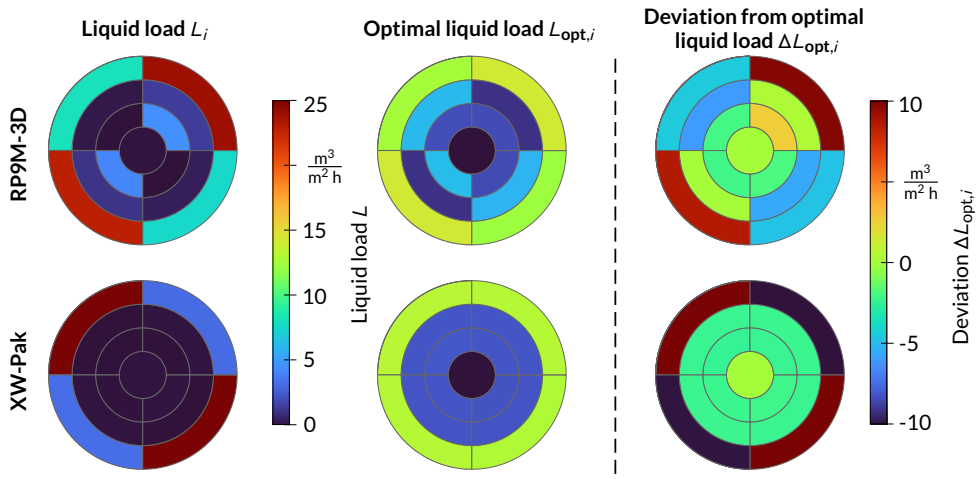

FIGURE 9 Local liquid load L_i over the segments (left), optimal local liquid load $L_{opt,i}$ over the segments (center) and deviation from the optimal local liquid load $\Delta L_{opt,i}$ (right). Top: RP9M-3D, bottom: XW-Pak.

crosspiece and wall circumference $C_{CP,i}$ in each segment better than is the case for the RP9M-3D.

When visualizing the results in ParaView, the spectra shown in Figure 9 help in locating areas inside the packing that disadvantageously distribute the liquid. These can be avoided while parts with advantageous characteristics can be amplified. The presented approach is considered to be a first step towards a knowledge-driven optimization of the design of such packings.

3.3 | Comparison with experimental data

Experiments to validate the simulation results were conducted at Ulm University using the test rig shown in Figure 10 with a setup loosely based on the work of Lämmermann et al. [8].

The experiments were conducted using *n*-heptane. The packing has a height $H_P = 540$ mm for RP9M-3D, 600 mm for the XW-Pak and a diameter $D_P = 20$ mm in both cases which matches the simulated packing structures. Vertical and horizontal guiding lines at the column wall and a laser are used to align the packing. A distributor with a single dripping point is connected to the top of the column. A liquid collector (see Fig. 11) with 13 segments that are of the same size as those in the simulations is installed directly beneath the packing. Column wall, packing, distributor and collector are separately manufactured using the AM method selective laser sintering with PA-12.

FIGURE 10 Test rig at Ulm University for the investigation of the liquid distribution inside packing geometries.

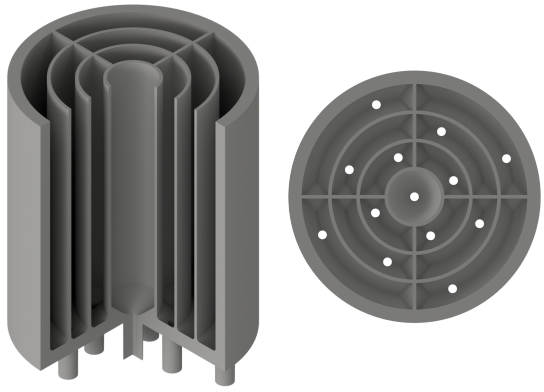

FIGURE 11 Side view (left) and top view (right) of the 13-segment liquid collector that is attached to the packing.

Figure 12 shows a simplified flowsheet of the setup. The membrane pump P–1 transports the liquid to the top of column C–1. The liquid flows through the packing and is distributed to the different segments of the collector. The fractions are merged in vessel V–2 and fed into the top of column C–1 until a steady state is reached after approximately 20 min. Once a steady state is reached, the liquid inside the segments is separately collected in vessels V–3 to V–15 for $\Delta t = 600$ s and weighted. Valve V–1 is a specially constructed AM device used to simultaneously switch the flow

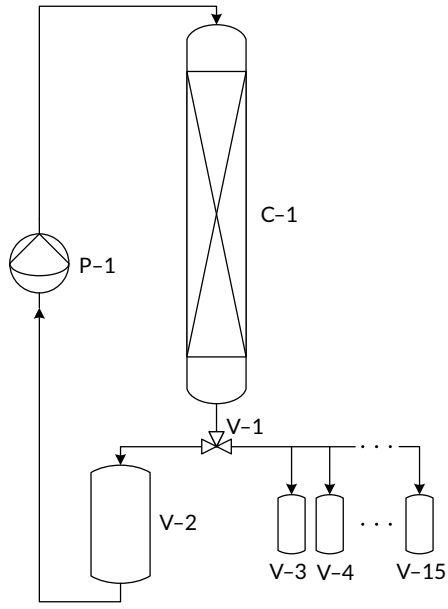

FIGURE 12 Simplified flowsheet of the test rig.

through all the segments from recirculation to measuring mode during operation of the test rig. In this way, the liquid flow in all segments can be measured simultaneously. The liquid load $L_{\mathrm{exp},i}$ in each segment is calculated as follows:

$$L_{\mathrm{exp},i} = \frac{M_i}{\rho \cdot A_i \cdot \Delta t}, \tag{15}$$

where ρ is the density of *n*-heptane, M_i the mass of liquid inside each segment and A_i the cross-sectional area of the segment.

The measurements were performed with liquid loads of $L_{\mathrm{overall,RP9M-3D}} \approx 7.2\ \mathrm{m^3\ m^{-2}\ h^{-1}}$ and $L_{\mathrm{overall,XW-Pak}} \approx 6.7\ \mathrm{m^3\ m^{-2}\ h^{-1}}$ for the RP9M-3D and XW-Pak, respectively. The liquid loads were slightly lower than the resulting loads in the simulations. For each packing, the experiments were repeated three times.

Figure 13 compares the simulated results of the liquid distribution for RP9M-3D and the XW-Pak with the experimentally obtained average results for each packing (left side). It furthermore depicts the deviation $\Delta L_{\mathrm{opt},i}$ of the local liquid loads L_i from their corresponding optimal local liquid loads $L_{\mathrm{opt},i}$ for the simulated and experimentally obtained values (right side).

All cases show the tendency of the liquid to flow towards the wall region. For the RP9M-3D, a sum of 62.5 $\mathrm{m^3\ m^{-2}\ h^{-1}}$

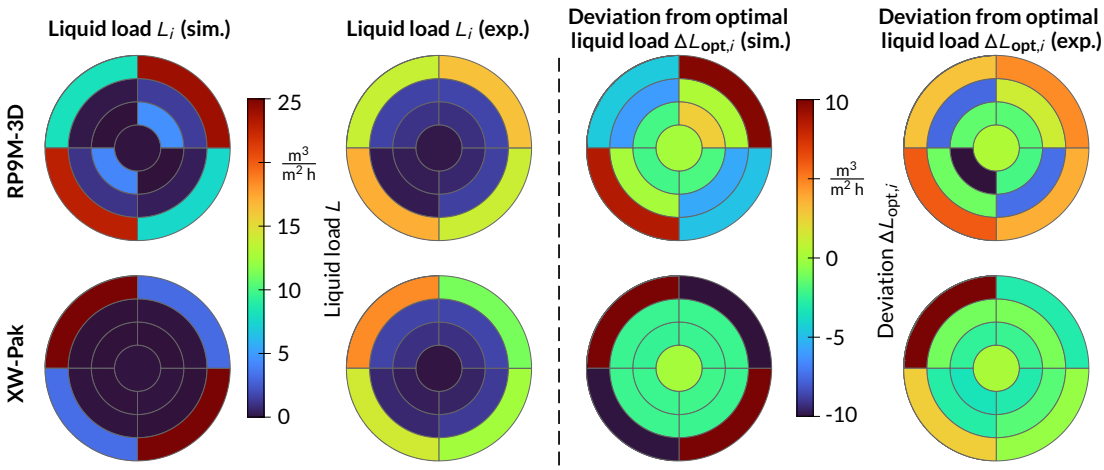

FIGURE 13 Simulated local liquid loads L_i (sim.) and experimental local liquid loads L_i (exp.) over segments (left) and deviation from the optimal local liquid load $\Delta L_{opt,i}$ (sim.) and (exp.) (right). Top: RP9M-3D, bottom: XW-Pak.

flows through the outer ring in the simulation and 61.3 $m^3\ m^{-2}\ h^{-1}$ in the experiment. In the XW-Pak, total liquid loads in the outer ring of 62.5 $m^3\ m^{-2}\ h^{-1}$ and 56.3 $m^3\ m^{-2}\ h^{-1}$ are reported for simulations and experiments, respectively. The simulation overestimates the amount of liquid in the outer ring for the XW-Pak by 10.9 %, while the liquid load at the wall for the RP9M-3D is slightly overestimated by 2.0 %. The deviations were calculated relative to the experimental values. For both structures, the simulations lead to a stronger separation of liquid in the outer ring resulting in two segments with a high and two segments with a low liquid load while the experiments show a less sharp separation of liquid loads in the outer ring. The main reason for this is that the segmentation boundaries of the lower end of the simulation domain are – in contrast to the experimental setup – infinitely thin. As the printed packing and collector have very small diameters of $D = 20$ mm, the separating walls with a thickness of 0.8 mm in Figure 11 occupy a space that is not negligible in relation to the cross section. This leads to coalescence effects resulting in a less sharp differentiation of the wall flow inside the experimental setup. Moreover, wall and packing structure are printed separately, which might increase the peripheral flow at the wall. Further deviations result from differences due to printing and post processing of the structures as well as from the finite length of the packings and the single point liquid distribution at the top. However, the experiments show that the XW-Pak yields smaller deviations from the optimal local liquid load $\Delta L_{opt,i}$ than the RP9M-3D (see Fig. 13). This matches the trend shown by the simulation results and in doing so, the core hypothesis underlying our simulation work. Despite showing some deviations in the liquid load distribution, the

experimentally obtained results support the conclusions drawn from the simulations.

4 | CONCLUSION

In this paper, the liquid flow inside different structured packings with enclosing wall is simulated for laboratory scale. A simulation technique that enables the prediction of the liquid phase and flow distributions over the structure surface in a quasi-steady state of the two-phase flow has been developed. It uses a periodic setup for a representative element of the structure. A two-step approach is proposed to ensure sufficient accuracy of the simulation results with reasonable computing times. The converged solution of a coarser numerical mesh is mapped onto a very fine mesh and the simulation resumed for another flow passage through the structure. Experimental results validate the simulations.

A new data processing tool, which takes into account the packing crosspiece arrangement, analyzes the liquid distribution as well as optimal liquid loads. The simulated liquid flow inside the newly designed structure XW-Pak matches its optimal liquid load distribution better than in the RP9M-3D case.

The generated spectra of the local liquid load distribution at the domain outlet segments are used to obtain a more insightful graphical visualization in ParaView, relating the obtained liquid distribution to an optimal one. This method confirmed the superiority of the XW-Pak over the RP9M-3D in this respect. The method can be used to further improve the design of additively manufactured packings with respect to the flow distribution over their cross-section. Such an optimization is crucial for the objectives of enhancing the separation efficiency of the column and the effectiveness of the whole scale-up process.

AUTHOR CONTRIBUTIONS

Nadin Sarajlic: Conceptualization; data curation; formal analysis; investigation; methodology; validation; visualization; writing - original draft; writing - review & editing. **Johannes Neukäufer:** Conceptualization; investigation; methodology; software; writing - review & editing. **Mohamed Adel Ashour:** Investigation; methodology; validation; writing - review & editing. **Thomas Grützner:** Conceptualization; funding acquisition; methodology; project administration; supervision; writing - review & editing. **Sebastian Meinicke:** Conceptualization; formal analysis; investigation; methodology; writing - review & editing. **Carsten Knösche:** Conceptualization; methodology; project administration; writing - review & editing.

Jürgen Paschold: Conceptualization; methodology. **Harald Klein:** Funding acquisition; methodology; supervision. **Sebastian Rehfeldt:** Conceptualization; funding acquisition; methodology; project administration; supervision; writing - review & editing.

NOMENCLATURE

| Latin symbols

Symbol	description, (unit)
A	area, $\left(\mathrm{m}^2\right)$
a	specific geometric surface area, $\left(\mathrm{m}^2\ \mathrm{m}^{-3}\right)$
C	packing crosspiece circumference, (m)
Co	Courant number, (–)
D	diameter, (mm)
$\mathbf{g}$	gravitational acceleration, $\left(\mathrm{m\,s}^{-2}\right)$
H	height, (mm)
h	holdup, (–)
L	liquid load, $\left(\mathrm{m}^3\ \mathrm{m}^{-2}\ \mathrm{h}^{-1}\right)$
M	mass, (kg)
p	pressure, (Pa)
t	time, (s)
$\mathbf{u}$	velocity, $\left(\mathrm{m\,s}^{-1}\right)$
$\mathbf{x}$	distance, (m)

| Greek symbols

Symbol	description, (unit)
α	liquid fraction, (–)
ε	void fraction, (–)
Θ	contact angle, (°)
κ	curvature, (–)
μ	dynamic viscosity, (Pa s)
ν	kinematic viscosity, $\left(\mathrm{m^2\,s^{-1}}\right)$
ρ	density, $\left(\mathrm{kg\,m^{-3}}\right)$
σ	surface tension, $\left(\mathrm{kg\,s^{-2}}\right)$
τ	stress tensor, (Pa)

| Subscripts

Symbol	description, (unit)
0	static; empty column
A	advancing
avg	average
CP	packing crosspiece (or wall)
exp	experimental
G	gravitational
g	gas
geo	geometric
i	segment *i*
l	liquid
opt	optimal
overall	overall (in steady state)
P	packing
R	receding
r	compression
σ	surface tension

REFERENCES

[1] Stichlmair JG, Klein H, Rehfeldt S. Distillation: Principles and Practice. Wiley; 2021. https://books.google.de/books?id=NTQtEAAAQBAJ.

[2] Eiden U, Kaiser R, Schuch G, Wolf D. Scale-up von Destillationskolonnen. Chemie Ingenieur Technik 1995;67(3):269–279.

[3] Neukäufer J, Sarajlic N, Klein H, Rehfeldt S, Hallmann H, Knösche C, et al. Flexible distillation test rig on a laboratory scale for characterization of additively manufactured packings. AIChE Journal 2021;p. e17381.

[4] Hofen W, Körfer M, Zetzmann K. Scale-up-Probleme bei der experimentellen Verfahrensentwicklung. Chemie Ingenieur Technik 1990;62(10):805–812.

[5] Hanusch F, Rehfeldt S, Klein H. Liquid Maldistribution in Random-Packed Columns: Experimental Investigation of Influencing Factors. Chemical Engineering & Technology 2018;41(11):2241–2249.

[6] Billet R. Packed towers in processing and environmental technology; 1995.

[7] Neukäufer J, Hanusch F, Kutscherauer M, Rehfeldt S, Klein H, Grützner T. Methodology for the development of additively manufactured packings in thermal separation technology. Chemical Engineering & Technology 2019;42(9):1970–1977.

[8] Lämmermann M, Schwieger W, Freund H. Experimental investigation of gas-liquid distribution in periodic open cellular structures as potential catalyst supports. Catalysis Today 2016;273:161–171.

[9] Qammar H, Gładyszewski K, Górak A, Skiborowski M. Towards the development of advanced packing design for distillation in rotating packed beds. Chemie Ingenieur Technik 2019;91(11):1663–1673.

[10] Bara JE, Hawkins CI, Neuberger DT, Poppell SW. 3D printing for CO 2 capture and chemical engineering design. Nanomaterials and Energy 2015;.

[11] Reitze A, Grünewald M, Riese J. Experimentelle Untersuchung additiv gefertigter strukturierter Packungen für Laborkolonnen. Chemie Ingenieur Technik 2020;92(9):1304–1305.

[12] Mardani S, Ojala LS, Uusi-Kyyny P, Alopaeus V. Development of a unique modular distillation column using 3D printing. Chemical Engineering and Processing: Process Intensification 2016 nov;109:136–148.

[13] Grinschek F, Xie D, Klumpp M, Kraut M, Hansjosten E, Dittmeyer R. Regular Microstructured Elements for Intensification of Gas–Liquid Contacting Made by Selective Laser Melting. Industrial & Engineering Chemistry Research 2019;59(9):3736–3743.

[14] Li C, Li J, Li D, Ma S, Li H. Experimental study and CFD numerical simulation of an innovative vapor splitter in dividing wall column. AIChE Journal 2020;66(8):e16266.

[15] Said W, Nemer M, Clodic D. Modeling of dry pressure drop for fully developed gas flow in structured packing using CFD simulations. Chemical Engineering Science 2011;66(10):2107–2117.

[16] Lautenschleger A, Olenberg A, Kenig E. A systematic CFD-based method to investigate and optimise novel structured packings. Chemical Engineering Science 2015;122:452–464.

[17] Bertling R, Hack M, Ausner I, Wehrli M, Kenig E. CFD Simulation of Film and Rivulet Flows on Microstructured Surfaces. In: Computer Aided Chemical Engineering, vol. 48 Elsevier; 2020.p. 61–66.

[18] Hirt CW, Nichols BD. Volume of fluid (VOF) method for the dynamics of free boundaries. Journal of computational physics 1981;39(1):201–225.

[19] Haroun Y, Raynal L, Alix P. Prediction of effective area and liquid hold-up in structured packings by CFD. Chemical Engineering Research and Design 2014;92(11):2247–2254.

[20] Olenberg A, Kenig E. Numerical investigation of liquid flow morphology in structured packings. Chemical Engineering Science 2020;219:115559.

[21] Ataki A, Bart HJ. Experimental and CFD simulation study for the wetting of a structured packing element with liquids. Chemical Engineering & Technology: Industrial Chemistry-Plant Equipment-Process Engineering-Biotechnology 2006;29(3):336–347.

[22] Hill S, Acher T, Hoffmann R, Ferstl J, Deising D, Marschall H, et al. Quantifizierung der Trenneffizienz einer strukturierten Packung mittels numerischer Simulation. Chemie Ingenieur Technik 2019;91(12):1833–1841.

[23] Macfarlan LH, Seibert AF, Phan MT, Eldridge RB. CFD-based study on structured packing geometry. Chemical Engineering Science 2021;243:116767.

[24] Macfarlan LH, Phan MT, Eldridge RB. Structured packing geometry study for liquid-phase mass transfer and hydrodynamic performance using CFD. Chemical Engineering Science 2022;249:117353.

[25] Reitze A, Grünewald M, Riese J. Characterization of Liquid-Phase Distribution in 3D Printed Structured Packings with an Enclosed Column Wall. Industrial & Engineering Chemistry Research 2021;.

[26] Foundation TO, OpenFOAM v9 User Guide;. Accessed: 2021-09-22. `https://cfd.direct/openfoam/user-guide`.

[27] Ferziger JH, Perić M, Street RL. Computational Methods for Fluid Dynamics. Springer; 2019.

[28] Berberović E, van Hinsberg NP, Jakirlić S, Roisman IV, Tropea C. Drop impact onto a liquid layer of finite thickness: Dynamics of the cavity evolution. Physical Review E 2009;79(3):036306.

[29] Deshpande SS, Anumolu L, Trujillo MF. Evaluating the performance of the two-phase flow solver interFoam. Computational science & discovery 2012;5(1):014016.

[30] Rusche H. Computational fluid dynamics of dispersed two-phase flows at high phase fractions. PhD thesis, Imperial College London (University of London); 2003.

[31] Brackbill JU, Kothe DB, Zemach C. A continuum method for modeling surface tension. Journal of computational physics 1992;100(2):335–354.

[32] Hill S, Acher T, Hoffmann R, Ferstl J, Rarrek A, Klein H. CFD simulation of the hydrodynamics in structured packings. In: Proceedings of the ICMF-2016–9th International Conference on Multiphase Flow; 2016. p. 22–27.

[33] Hattori T, Koshizuka S. Numerical simulation of droplet behavior on an inclined plate using the Moving Particle Semi-implicit method. Mechanical Engineering Journal 2019;p. 19–00204.

[34] Feng JQ. A computational study of high-speed microdroplet impact onto a smooth solid surface. arXiv preprint arXiv:160207672 2016;.

[35] MATLAB. 9.10.0.1602886 (R2021a). Natick, Massachusetts: The MathWorks Inc.; 2021.

[36] Buhlmann U, Packing for material exchange columns, and process for producing the packing. Google Patents; 1985. DE Patent App. 8,282,105,106 T.

[37] Macdougall G, Ockrent C. Surface energy relations in liquid/solid systems I. The adhesion of liquids to solids and a new method of determining the surface tension of liquids. Proceedings of the Royal Society of London Series A Mathematical and Physical Sciences 1942;180(981):151–173.

[38] Neukäufer J, Seyfang B, Grützner T. Investigation of Contact Angles and Surface Morphology of 3D-Printed Materials. Industrial & Engineering Chemistry Research 2020;59(14):6761–6766.

[39] Lemmon EW, Bell IH, Huber ML, McLinden MO, NIST Standard Reference Database 23: Reference Fluid Thermodynamic and Transport Properties-REFPROP, Version 10.0, National Institute of Standards and Technology; 2018. https://www.nist.gov/srd/refprop.

[40] Mohsen-Nia M, Rasa H, Naghibi S. Experimental and theoretical study of surface tension of n-pentane, n-heptane, and some of their mixtures at different temperatures. The Journal of Chemical Thermodynamics 2010;42(1):110–113.

[41] Deibele L, Dohrn R. Miniplant-Technik: in der Prozessindustrie. Wiley; 2012. https://books.google.de/books?id=mTwBRZlpvlAC.